An ONIOM study on the enantioselective Diels–Alder reaction catalyzed by SiO$_2$ – Immobilized chiral oxazaborolidinium cation

Nasr Y.M. Omar, Noorsaadah A. Rahman, Sharifuddin Md Zain*

Department of Chemistry, University of Malaya, 50603 Kuala Lumpur, Malaysia

ABSTRACT

The mechanism and enantioselectivity of the Diels–Alder reaction between 2-methyl-1,3-butadiene and 2,3-dimethyl-1,4-benzoquinone catalyzed by SiO$_2$-supported chiral cationic oxazaborolidinium catalyst were investigated by the hybrid ONIOM(B3LYP/6-31G(d):UFF) method. The amorphous silica bulk was obtained by classical molecular dynamics using the melt-quench method and the heterogeneous surface was created by cleaving the bulk structure. The resultant amorphous silica surface was found to closely resemble silicas thermally treated at 673 K. The organocatalytic Diels–Alder reaction on the silica surface was observed to proceed via a concerted but highly asynchronous mechanism. The preferred transition state was found to correspond to an *endo* arrangement of the diene and the catalyst-coordinated benzoquinone, and the enantioselectivity was calculated to be 86.5% at 298 K. The mechanism and enantioselectivity of the studied reaction were generally comparable to those observed for the homogeneous catalyst.

© 2010 Elsevier B.V. All rights reserved.

1. Introduction

Organic synthesis on solid-phase has been receiving an increasing attention in the community of synthetic organic chemists as a method for carrying out chemical reactions with high regio- and/or stereoselectivity under environmentally benign, solvent-free conditions. The solid-phase approach to enantioselective synthesis has proven suitable for a number of enantioselective reactions [1]. Various support materials have been used for solid-phase organic synthesis including polystyrene, polysaccharides, and silica [2].

Heterogeneous catalysis is important in many industrial processes for fine chemicals synthesis [3]. Heterogenization by immobilizing a homogeneous catalyst on a solid support is a strategy that attempts to combine the advantages of homogeneous catalysis (e.g., high enantioselectivity) with the advantages of heterogeneous catalysis such as the ease of separation of the catalyst from the product, the reusability of the catalyst and the reduction in cost [3–5]. Catalyst immobilization methods [3,5–10] can be classified mainly into two groups, namely, covalent and non-covalent immobilization. Solid supports used include organic polymeric materials (e.g., polystyrene resins) and inorganic solids such as silica and zeolites.

Silica- and organic polymer-immobilized catalysts such as transition-metal complexes with chiral ligands and chiral organocatalysts are now commonplace in enantioselective organic synthesis involving numerous types of organic reactions [11–35]. The enantioselective Diels–Alder reaction is a versatile tool for the synthesis of pharmaceutical and natural products. An important class of heterogeneous catalysts for enantioselective Diels–Alder reaction is concerned with chiral Lewis acids (both organic and inorganic) anchored to organic polymeric or inorganic solid materials [11–20].

Oxazaborolidines attached to polystyrene resin [26,27,29] and to silica [34,36] are among numerous chiral organocatalysts that have been used in enantioselective heterogeneous catalysis. Their main use was the enantioselective reduction of ketones. However, the use of solid-supported oxazaborolidine catalysts for the Diels–Alder reaction has not been reported.

The Diels–Alder reaction of quinones is highly useful in the synthesis of many complex natural products. An example of an enantioselective Diels–Alder reaction utilizing the chiral oxazaborolidinium cation catalyst **3** has been shown by Corey in a reaction between 2-methyl-1,3-butadiene (isoprene) **1** and 2,3-dimethyl-1,4-benzoquinone **2** [37,38] as shown in Fig. 1.

In the current study, the Diels–Alder reaction between **1** and **2** in the presence of amino silica-immobilized model catalyst **4** is computationally investigated. The emphasis is mainly to gain an understanding of the mechanism and enantioselectivity of this solid-phase reaction which can be later tested experimentally.

* Corresponding author. Tel.: +60 3 7967 4442; fax: +60 3 7967 4442.
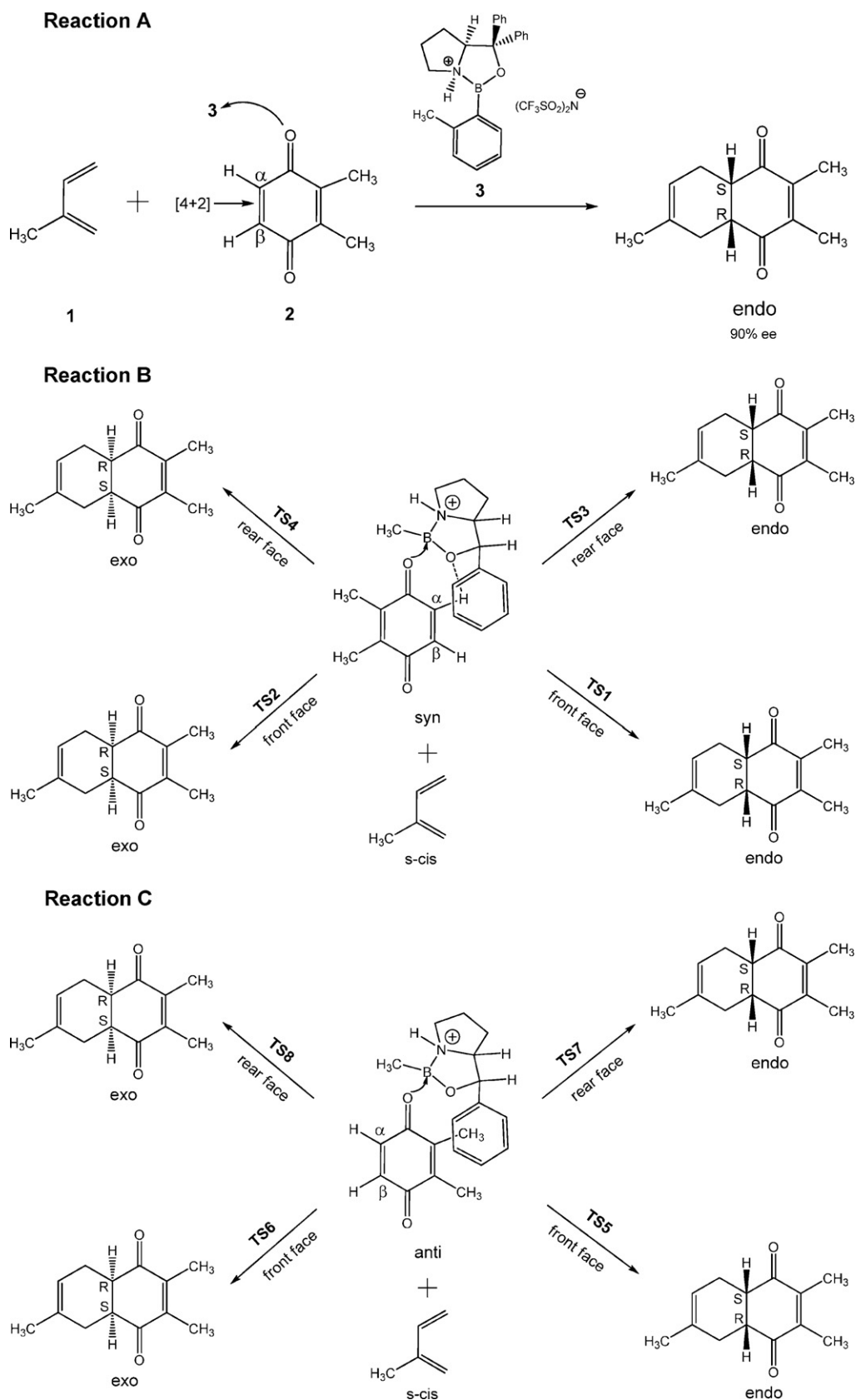*E-mail address:* smzain@um.edu.my (S.M. Zain).

Fig. 1. (a) Corey's enantioselective Diels–Alder reaction of benzoquinone using homogeneous chiral oxazaborolidinium catalyst, (b) catalyzed Diels–Alder reaction with four possible reaction pathways with the catalyst coordinated *syn* to the HC=CH double bond that undergoes the [4+2]-cycloaddition, and (c) catalyzed Diels–Alder reaction with four possible reaction pathways with the catalyst coordinated *anti* to the HC=CH double bond that undergoes the [4+2]-cycloaddition.

The mechanism and enantioselectivity are also compared to those observed for the homogeneous catalyst.

4
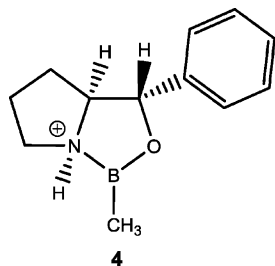
2. Computational details

2.1. Preparation of amorphous silica bulk and surface

Classical molecular dynamics simulations were carried out using the SageMD2 software package [39]. The model of bulk amorphous silica was generated by classical molecular dynamics using the well-established melt-quench method (see below) [40–57]. The building of amorphous silica bulk and surface is illustrated in Fig. 2.

All simulations were carried out using the velocity Verlet integration algorithm with an integration time step of 1.6 fs and employing periodic boundary conditions. The Berendsen thermostat and barostat were used for controlling the temperature and the pressure. The potential used for these simulations is a two-body interatomic potential [46–48] as shown in Eq. (1)

$$U(r) = \frac{q_k q_l}{r} + U_0[e^{-2\alpha(r-r_0)} - 2e^{-\alpha(r-r_0)}] \qquad (1)$$

where q_k and q_l are the charges on atoms k and l; r is the distance between atoms k and l; and U_0 (the potential well depth), α (the potential width control parameter) and r_0 (the equilibrium interatomic distance) are the adjustable Morse potential parameters. These Morse potential parameters are listed in Table 1 [46–48]. Cutoff distances for Morse interactions were set to 9 Å. Electrostatic interactions were calculated by Ewald summation method with a real space cutoff distance of 7 Å. The charges used are +1.30 and −0.65 for the Si and O atoms, respectively [47,48].

To construct bulk amorphous silica, a β-cristobalite unit cell (Si_8O_{16}) was replicated $4 \times 4 \times 4$ times to produce a cubic supercell ($28.6 Å \times 28.6 Å \times 28.6 Å$) of 1536 atoms ($Si_{512}O_{1024}$). The cooling cycle 1-I suggested by Huff et al. [45] was then followed. It started with an NVT simulation at 8000 K for 20 ps to remove any memory of the initial atomic configuration followed by NVT simulations at 4000 K, 2000 K and 1000 K. At each temperature step, the simulation was run for 20 ps. A 10 ps of NVT dynamics at 300 K and then a 30 ps of NPT simulation at 300 K and 1 atm pressure completed the cycle.

To create the amorphous silica surface, the bulk amorphous silica was cleaved in the middle along the *Y*-direction. The resultant slab (∼14 Å in thickness) was taken to produce the amorphous silica surface. A few atoms were taken out from the system to keep its electroneutrality and the final slab consisted of 246 SiO₂ units. The system was made periodic in three dimensions by placing a vacuum of 42 Å (i.e. ∼3 times the slab thickness) on top of the silica surface. This enables the use of Ewald summation method and the long vacuum gap usually reduces the unwanted interactions

Table 1
Morse potential parameters for silica.

	U_0 (eV)	α (1/Å)	r_0 (Å)
Si–Si	0.007695	2.0446	3.7598
Si–O	1.99597	2.6518	1.6280
O–O	0.023272	1.3731	3.791

between the silica surface and the periodic images. Atoms situated within 3 Å from the bottom of the slab in the *Y*-direction were fixed during the simulation. The slab was then annealed using the same potential used for creating the bulk amorphous silica (Eq. (1)). A 10 ps NVT dynamics at 1500 K followed by an NVT simulation at 300 K for 10 ps resulted in the desired amorphous silica surface.

The final silica surface defects (i.e. undercoordinated or overcoordinated atoms) depend on the choice of the initial simulation temperature and the thickness of the immobilized atoms [40,43]. Higher simulation temperature and thinner layer of immobilized atoms usually yield lower surface defects. An important factor for choosing the initial simulation temperature is the glass transition temperature below which no structural changes in silica are observed [55]. Using the same potential employed in the current study (Eq. (1)), Takada et al. [47] estimated the glass transition temperature to be 1400 K. Hence, to allow structural changes, an initial simulation temperature of 1500 K was selected in this study. As for the simulation time, it has been shown that the concentration of the silica surface defects becomes stable with little or no changes after 10 ps [44]. In another study, a simulation time of ∼1 ps was reported adequate to produce the surface defects [57]. Therefore, in this study, a simulation time of 10 ps was chosen. The combination of the initial simulation temperature of 1500 K, the simulation time of 10 ps and the immobilization of the atoms situated within 3 Å from the bottom of the slab yielded the desired amorphous silica surface (cf. Section 3.1).

2.2. Details of the gas-phase calculations (homogeneous catalyst)

In the Diels–Alder Reaction A (Fig. 1), there is a pair of possible enantiomers of the catalyst **3**, either the *S* or the *R* stereoisomer. In addition, there are two rotamers for each configuration resulting from the rotation about the B-*o*-tolyl bond. Besides, there are two possible sites (double bonds) on the benzoquinone that the diene can attack approaching from either the front or the rear face. Moreover, the catalyst coordination to the benzoquinone can be *syn* or *anti* to the HC≡CH subunit that undergoes the [4+2]-cycloaddition. Since there are two stereogenic carbons in the products, there will be up to four diastereomeric transition states ((*S,R*), (*R,S*), (*R,R*), and (*S,S*)). Fortunately, in this reaction, there is no issue of regioselectivity since 2,3-dimethyl-1,4-benzoquinone is C_2 symmetric. Also, the two benzoquinone oxygens are equally available for catalyst coordination. Thus, there would be numerous possible pathways for this reaction to proceed.

To simplify matters, the model catalyst **4** is used throughout this investigation. This catalyst eliminates the need for the rotamers mentioned above to be considered and reduces the computational cost as it requires smaller number of basis functions compared to the catalyst **3**. The (*S*)-enantiomer of the catalyst **4** is used since it is the more commonly used enantiomer in experimental studies [38,58–65]. As for the possible diastereomeric products, only the enantiomeric pair (*S,R*) and (*R,S*) is considered in the current work since the (*S,R*)-enantiomer is the major product observed experimentally (Fig. 1) [37,38]. Also, only the addition of the diene to the less substituted double bond of the benzoquinone is studied here since this addition will lead to the product observed experimentally [37,38]. The studied pathways for this reaction are illustrated in Fig. 1.

Geometry optimizations and vibrational frequencies of the reactants, transition states and products were carried out *in vacuo* using density functional theory with the B3LYP functional and the 6-31G(d) basis set as implemented in the Gaussian 03 program [66].

Prior to B3LYP/6-31G(d) calculations, all equilibrium and transition states were optimized and characterized using the AM1 semiempirical method followed by B3LYP/3-21G calculations. This often allows reaching better structures and reduces the total num-
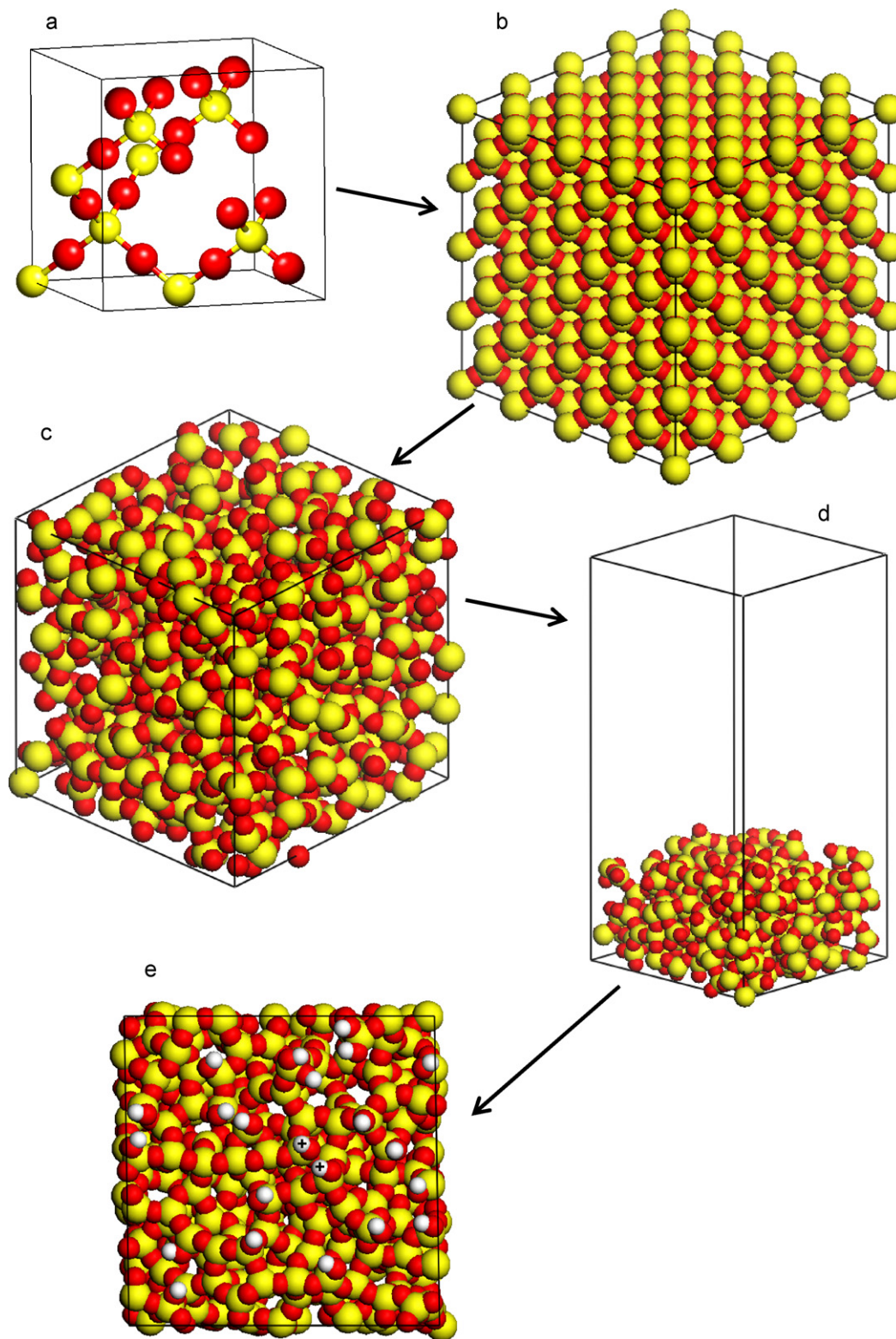
Fig. 2. Building amorphous silica bulk and surface. (a) β-Cristobalite unit cell, (b) β-cristobalite supercell, (c) created bulk amorphous silica, (d) final amorphous silica surface, and (e) final amorphous silica surface with silanol groups (top view). The two hydrogen atoms with the '+' sign indicate where the functionalization of the surface will take place. Silicon, oxygen and hydrogen atoms are displayed in light gray, dark gray and white (yellow, red and white on the Web), respectively.

ber of steps required at the higher level of theory. The default SCF algorithm (EDIIS/CDIIS) in the Gaussian 03 program was used unless in case of convergence problem, in particular for transition states, where the keyword "scf=(maxconventionalcycles=20,xqc)" was used. This keyword instructs the program to use the default SCF algorithm for the first 20 cycles then to use the quadratically convergent (QC) SCF algorithm in order to ensure convergence. Geometry optimizations to local minima and transition states were accomplished with the Berny algorithm in redundant internal coordinates without any symmetry restriction.
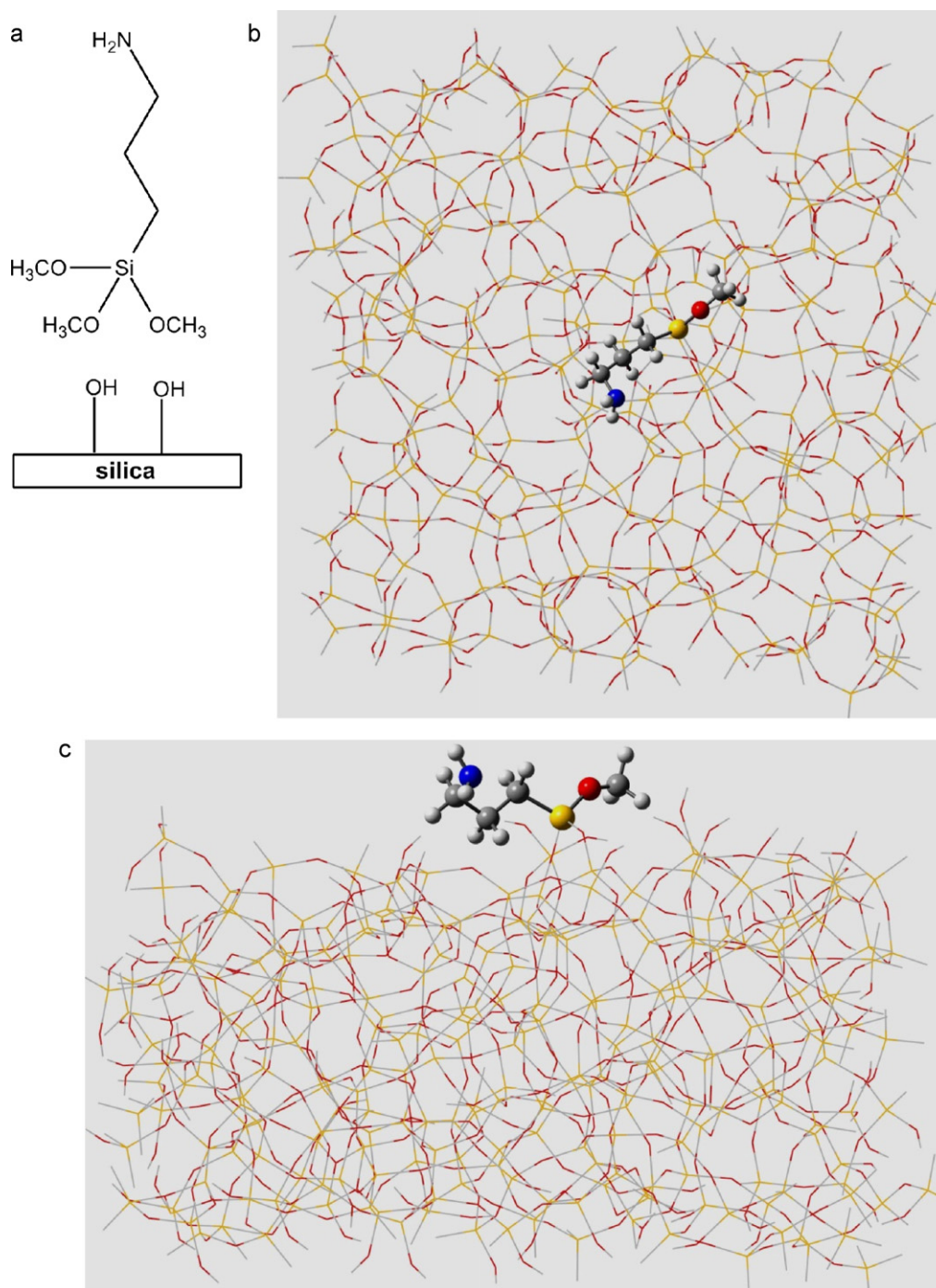
Fig. 3. Amino silica surface. (a) 3-Aminopropyltrimethoxysilane to be attached to the silica surface, (b) UFF optimized amino silica surface (top view), and (c) UFF optimized amino silica surface (side view). Hydrogens were used to fill out the valence that resulted from removing the periodic boundary conditions. Hydrogens were added using the HyperChem program [68]. Color code: carbon, silicon, hydrogen, oxygen and nitrogen are in moderate gray, light gray, white, and dark gray (gray, yellow, white, red and blue on the Web), respectively.

Vibrational frequency calculations were performed at the optimized geometries to verify whether the obtained structures are minima or transition states as well as to determine zero-point vibrational energies and thermochemical quantities. The vibration associated with the imaginary frequency was ensured to correspond to a displacement in the direction of the reaction coordinate. This was achieved with the graphical user interface for Gaussian program (GaussView). The zero-point vibrational energies and thermochemical quantities were calculated using frequencies scaled by 0.9804. Thermochemical quantities were calculated at 298 K and at 1.0 atm pressure.

According to Boltzmann statistics, the fraction X of a molecule M having a specific geometry at temperature T can be given by

$$X_M = \frac{e^{-G_M/RT}}{\sum_m e^{-G_M/RT}} \qquad (2)$$

where m runs over all possible geometries, each characterized by its Gibbs free energy G. In this study, Eq. (2) is used to compute the fraction of an optimized *endo* or *exo* transition state with respect to all optimized *endo* or *exo* transition states.

2.3. ONIOM models and details of the solid-phase calculations (heterogeneous catalyst)

Modeling heterogeneous catalytic systems is typically performed using one of three different representations of the catalyst: clusters, embedded clusters or slabs [67]. In the present work, the slab model was used. 3-Aminopropyltrimethoxysilane (a commonly used grafting molecule) was attached to the generated amorphous silica surface (Fig. 2e) to produce an aminopropyl-functionalized silica surface (Fig. 3). The model chiral cationic oxazaborolidinium catalyst **4** was then covalently immobilized on the amino silica surface (Fig. 4).

All ONIOM(QM:MM) calculations were performed *in vacuo* using the Gaussian 03 program [66]. Density functional theory with the B3LYP functional and the 6-31G(d) basis set was chosen as the QM method while the 'universal force field' (UFF) [69] was selected as the MM method. The UFF atom types for the Si and O atoms

that are part of the silica slab were specified explicitly with Si3 for Si and O_3_z for O. For the remaining atoms in the system, the UFF atom types automatically assigned by the Gaussian 03 program were accepted. The molecular connectivity was also explicitly specified (keyword "geom=connectivity").

No charges were assigned to the MM atoms and the electrostatic interactions at both the MM and QM levels are, thus, ignored in the current study. The UFF does not include default values for partial charges. For determining the partial charges, the use of the charge equilibration procedure (QEq) might be suitable [70]. In this procedure, the computed charges are allowed to adjust to geometrical changes. However, it has been shown that the performance of the UFF without charges is better than the UFF combined with QEq [71]. In addition, in the Gaussian program, the QEq partial charges are calculated only at the initial geometry and are not updated during the course of geometry optimization [72]. Since charges depend on structural parameters, the electrostatic interactions will not be calculated accurately using charges derived from the initial structure. In an embedded cluster ONIOM(QM:MM) study on the cyclization of C6 diene in zeolites, Joshi and Thomson [73] concluded that the MM partial charges caused nearly constant shifts in the energetics, and not necessarily in a stabilizing manner. Furthermore, since the ONIOM method neglects the polarization of the MM region, the effect of the MM charges will be overestimated [74]. The ONIOM method with the mechanical embedding scheme (ONIOM-ME) is therefore used for all calculations.

In the Gaussian 03 program, the default algorithm used for ONIOM(QM:MM) geometry optimization to a minimum is different than the algorithm used for optimization to a transition-state structure. In the geometry optimization to a minimum, ONIOM(QM:MM) takes advantage of the microiterations procedure [75] that allows the use of a fast MM optimizer so that the entire MM layer is fully minimized at each geometry optimization step of the QM layer. This is a computationally efficient procedure that allows faster geometry optimization than the 'normal' procedure which includes all atoms in the geometry optimization similar to a regular non-ONIOM calculation. In the Gaussian 03 program, the 'normal' procedure is the only procedure available for optimization to a transition-state structure. Therefore, ONIOM(QM:MM) transition-state structure searches are computationally demanding.

Vibrational frequency calculations were carried out at the optimized geometries to verify whether the obtained structures are minima or transition-state structures as well as to determine zero-point vibrational energies and thermodynamic quantities. The vibration associated with the imaginary frequency was ensured to correspond to a displacement in the direction of the reaction coordinate. The zero-point vibrational energies and thermodynamic quantities were computed using frequencies scaled by 0.9804. Thermodynamic quantities were calculated at 298 K and at 1.0 atm pressure.

3. Results and discussion

3.1. Characterization of the amorphous silica bulk and surface

In this section, the amorphous silica bulk and surface are characterized. The characterization approach followed is simple rather than exhaustive. The density of the bulk amorphous silica obtained in this study is 2.25 g/cm^3, a value close to the experimental density of 2.20 g/cm^3 [76,77].

On the silica surface (Fig. 2d), the non-bridging oxygens (i.e. oxygen atoms bonded to less than two silicon atoms) density is 1.9/nm^2. The tricoordinated silicon atoms density is 0.9/nm^2. To obtain a hydroxylated surface, hydrogens were added to non-bridging oxygens and hydroxyl groups to tricoordinated silicons.
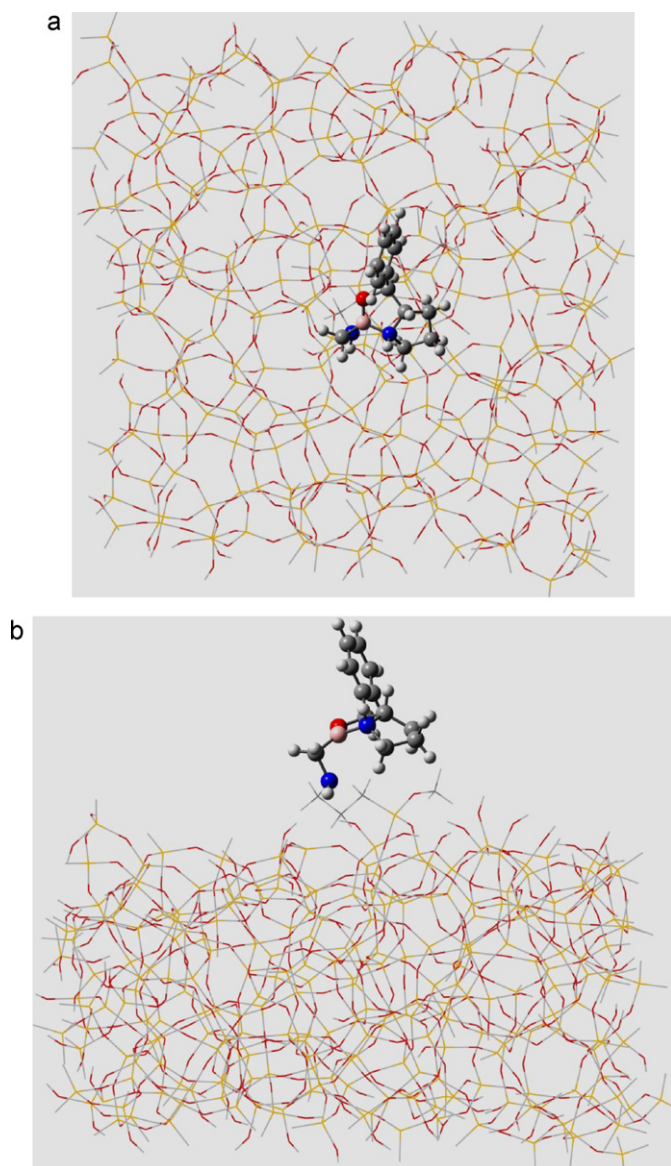

Fig. 4. ONIOM(B3LYP/6-31G(d):UFF) optimized amino silica-immobilized catalyst **4**. (a) Top view and (b) side view. The QM layer is in the ball-and-stick representation and the MM layer is in the wireframe representation. Color code: carbon in moderate gray, silicon in light gray, boron in light gray, hydrogen in white, oxygen in dark gray and nitrogen in dark gray. Color code on the Web: carbon in gray, silicon in yellow, boron in pink, hydrogen in white, oxygen in red and nitrogen in blue.
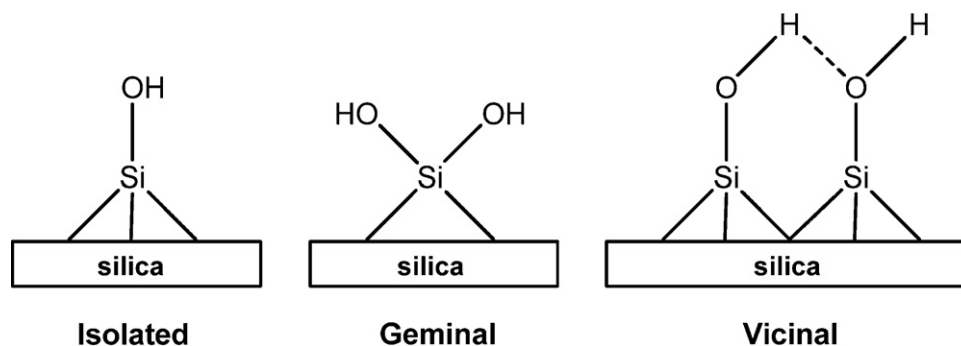
Fig. 5. Silanol groups on the surface of silica.

This resulted in a surface (Fig. 2e) having a silanol number (i.e. the number of hydroxyl groups per square nanometer) of 2.8 OH/nm^2. This silanol number is close to the silanol number obtained for thermally treated silica at 673 K ($\sim$3 OH/nm^2) [76,78]. Silica calcined at 673 K has been used as a solid support for organometallic catalysts [17,20].

The surface chemistry of silica is dominated by the surface silanol groups that participate in adsorption of molecules (e.g., water) as well as chemical modification of silica surfaces [78]. Types of silanol groups on the surface of silica include isolated, geminal and vicinal (or H-bonded) silanols (Fig. 5). At low temperatures, vicinal silanols almost entirely cover the surface [79]. Dehydroxylation of the silica surface begins at temperatures above 473 K and the silanol number decreases with increasing temperature. Vicinal silanols may remain on the silica surface up to $\sim$723 K, geminal silanols up to $\sim$1073 K, and isolated silanols up to $\sim$1273 K [76]. The ratio of the isolated silanols to geminal silanol groups on the silica surface is estimated to be $\sim$85/15 at temperatures in the range of 723–1073 K [76]. In the current work, the percentages of isolated, geminal and vicinal silanols are found to be 73%, 18% and 9%, respectively. This indicates that the simulated silica obtained in the present work corresponds to silica obtained by thermal treatment at temperatures close to 723 K, in line with the conclusion reached by using the silanol number.

In their experiment regarding the enantioselectivity of Diels–Alder reactions on SiO$_2$-immobilized Cu-bis(oxazoline) catalyst, Tanaka et al. [17] recommended that the loading of the catalyst is controlled to be at 0.1 mol/nm^2. This would allow the organofunctionalization of the silica surface surrounding the catalyst. As mentioned in Section 2.3, one molecule of catalyst **4** was covalently attached to the amino silica surface (Fig. 4). The loading of catalyst **4** on the silica surface is therefore 0.12 mol/nm^2. Furthermore, as stated in the 'specification sheet' for 3-aminopropyl-functionalized silica [80], 9% of the surface active groups are functionalized. This corresponds to two silanol groups for the silica surface obtained in this study. Hence, only one molecule of 3-aminopropyltrimethoxysilane was attached to the silica surface and the silica surface obtained in the current work is considered to be a good representative model and attachment of additional molecules of catalyst **4** to the silica surface was not necessary.

3.2. Gas-phase Diels–Alder reaction

The B3LYP/6-31G(d) optimized structures of the reactants are shown in Fig. 6 . The *syn* **R4** and *anti* **R5** coordination complexes between benzoquinone **R2** and catalyst **R3** are also shown in Fig. 6. A stronger coordination is observed for the *syn* complex having a B–O bond length shorter by 0.06 Å than that of the *anti* complex.

In addition, the *syn* complex shows a nonconventional hydrogen bond [81,82] between the C$_\alpha$–H hydrogen and the catalyst oxygen with 2.27 Å bond length. The stronger coordination in addition to the presence of hydrogen bonding in the *syn* complex led to a 7.1 kcal/mol stabilization for the *syn* complex as compared to the *anti* complex. This corresponds to almost a 100% of the Boltzmann population being represented by the *syn* complex. Furthermore, the Gibbs free energy for the *syn* coordination complex is lower than that of the separated reactants (**R2** + **R3**) by 4.4 kcal/mol. The *anti* coordination complex, however, is unfavored since the complex free energy is 2.7 kcal/mol higher than that of the separated reactants.

Shown in Fig. 6 are the B3LYP/6-31G(d) computed transition-state structures for the catalyzed Reactions B and C. The *syn* transition-state structures are more stable than their *anti* counterparts by about 3.3–9.9 kcal/mol. For both *syn* and *anti* transition-state structures, the B–O bond length is shorter (on average) than that of the reactant by 0.07 Å and 0.11 Å, respectively indicating stronger complexation at the transition state. A relatively stronger coordination is observed for the *syn* transition-state structures with B–O bond lengths shorter by about 0.01–0.04 Å than those of the *anti* transition-state structures. As in the case of the reactants, the *syn* transition-state structures possess a nonconventional hydrogen bond between the C$_\alpha$–H hydrogen and the catalyst oxygen with bond lengths in the range of 2.40–2.53 Å.

For the *endo* transition states, the lowest energy transition state is **TS1** representing $\sim$90.02% of the Boltzmann population of the *endo* transition states. This transition state involves the diene addition to the front face of the α,β double bond of the benzoquinone and the catalyst is coordinated *syn* to this bond. The next lowest transition state **TS3** has $\sim$9.94% of the Boltzmann population of the *endo* transition states. It is similar to **TS1** but the diene addition is to the rear face of the α,β double bond of the benzoquinone. The remaining 0.04% is due to **TS7**, which is similar to **TS3** but with the catalyst coordinated *anti* to the α,β double bond that undergoes the cycloaddition. As for the *exo* transition states, **TS4** represents the most stable transition state with $\sim$99.18% of the Boltzmann population of the *exo* transition states. It is similar to **TS3** except that the arrangement is *exo*. The remaining 0.82% is for **TS2**, which is similar to **TS4** but with the diene addition to the front face of the α,β double bond of the benzoquinone. The percent enantiomeric excess (%*ee*) is calculated to be 80.5% at 298 K favoring the *endo* product.

The average degree of asynchronicity for the transition-state structures is calculated to be 0.93 Å (Fig. 6). Thus, these transition-state structures point to concerted but highly asynchronous reaction pathways where the bond between the diene and carbon β of the dienophile is being formed in a larger extent than the bond between the diene and carbon α of the dienophile. The

asynchronicity can be explained by the frontier molecular orbital (FMO) theory [83,84]. For instance, the high degree of asynchronicity (0.99 Å) found in the transition-state structure **TS1** is due to the LUMO having much larger coefficient on the β carbon of the benzoquinone causing it to be much more electrophilic than the α carbon (the β carbon possesses 12.9% of the LUMO while the α carbon has only 2.0% of the LUMO). This results in a much larger overlap between the β carbon and the diene HOMO leading to a much stronger and shorter bond at the transition-state structure.
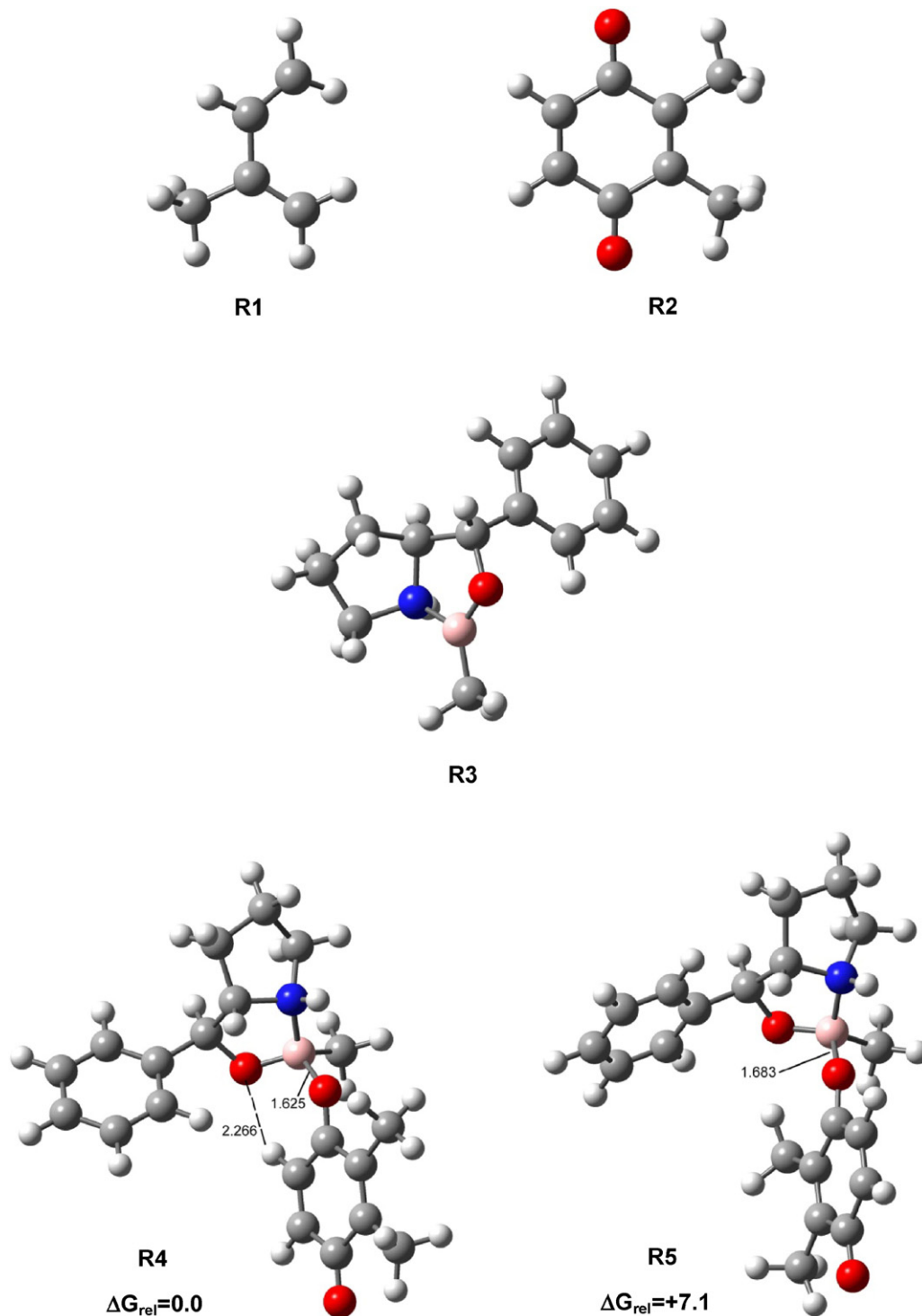

Fig. 6. B3LYP/6-31G(d) optimized reactants and transition-state structures for Reactions B and C. Relative free energies are in kcal/mol at 298 K. Distances are in Å. **TS1** = *endo* transition state involving diene attack to the front face, **TS2** = *exo* transition state involving diene attack to the front face, **TS3** = *endo* transition state involving diene attack to the rear face **TS4** = *exo* transition state involving diene attack to the rear face, **TS5** = *endo* transition state involving diene attack to the front face, **TS6** = *exo* transition state involving diene attack to the front face, **TS7** = *endo* transition state involving diene attack to the rear face and **TS8** = *exo* transition state involving diene attack to the rear face. Negative wavenumbers are imaginary frequencies. The color code is the same as in Fig. 4.
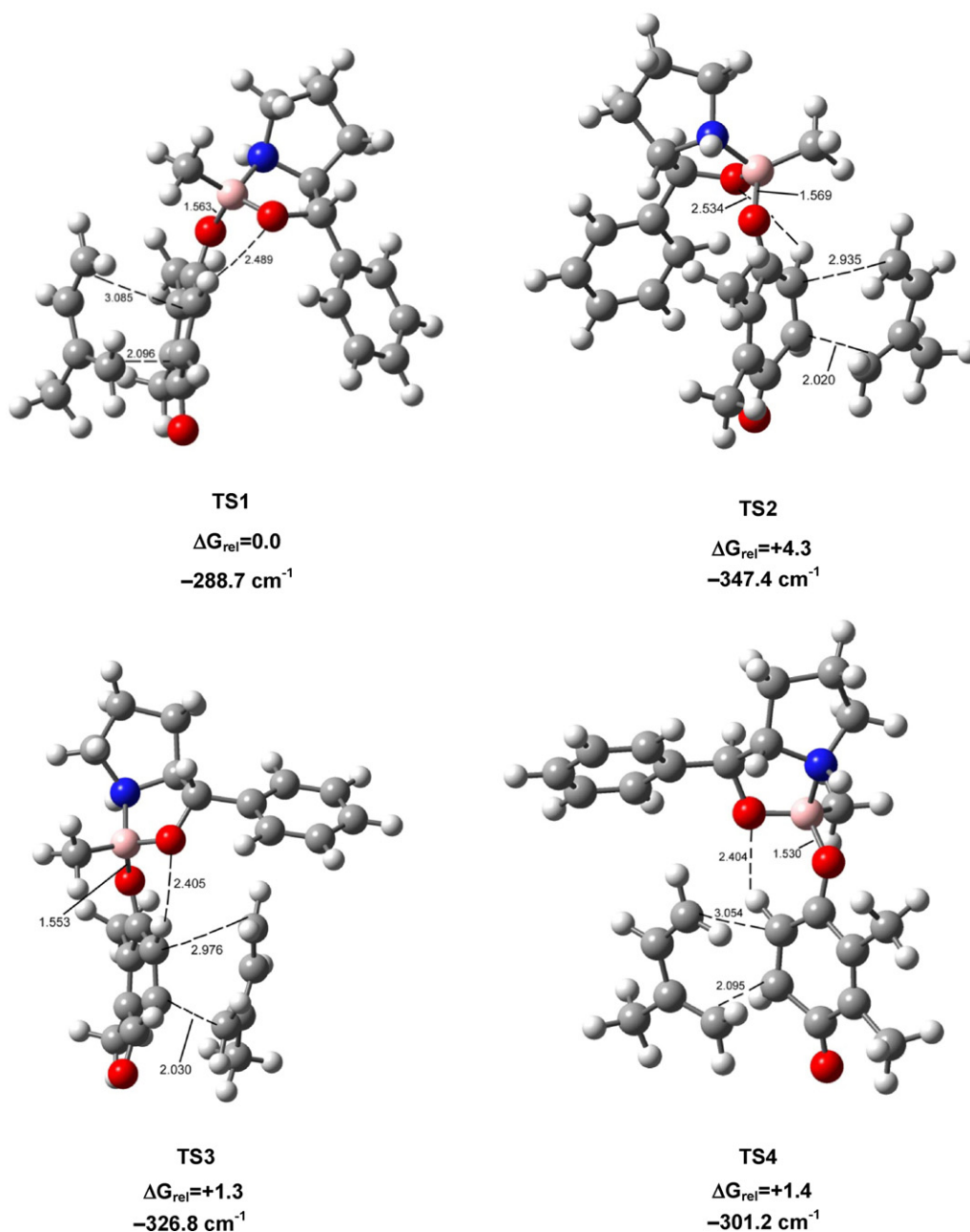
TS1

$\Delta G_{rel} = 0.0$

-288.7 cm^{-1}

TS2

$\Delta G_{rel} = +4.3$

-347.4 cm^{-1}

TS3

$\Delta G_{rel} = +1.3$

-326.8 cm^{-1}

TS4

$\Delta G_{rel} = +1.4$

-301.2 cm^{-1}

Fig. 6. (*Continued*).

3.3. Diels–Alder reaction on the silica surface

The Diels–Alder reaction studied on the silica surface is between isoprene **1** and 2,3-dimethyl-1,4-benzoquinone **2** in the presence of amino silica-supported catalyst **4** as shown in Fig. 7. Since optimization to a transition-state structure in ONIOM(QM:MM) is computationally demanding, only the *syn* transition-state structures are considered in this study. This choice is based on the results obtained for the gas-phase (Section 3.2 and Fig. 6) which indicated the *syn* transition-state structures to be more stable than the *anti* transition-state structures. In addition, the *syn* coordination between benzoquinone **2** and amino silica-immobilized catalyst **4** is found to be stronger than the *anti* coordination and the B–O bond length for the *syn* coordination complex is shorter by 0.03 Å than that of the *anti* complex. The *syn* complex also has a nonconven-

tional hydrogen bond between the C_α–H hydrogen and the oxygen of the catalyst with 2.66 Å bond length. This stronger coordination combined with the presence of hydrogen bonding in the *syn* coordination complex resulted in an 11.6 kcal/mol stabilization for the *syn* complex as compared to the *anti* complex which corresponds to a 100% of the Boltzmann population being represented by the *syn* complex. Furthermore, the *anti* coordination is unfavored since the complex Gibbs free energy is 6.2 kcal/mol higher than that of the separated reactants. On the other hand, the free energy for the *syn* coordination complex is lower than that of the separated reactants by 5.4 kcal/mol and is therefore strongly favored over the *anti* coordination complex.

The ONIOM(B3LYP/6-31G(d):UFF) optimized transition states are shown in Fig. 8. The B–O bond length (on average) at the transition states is shorter than that of the reactant by 0.02 Å indicating a
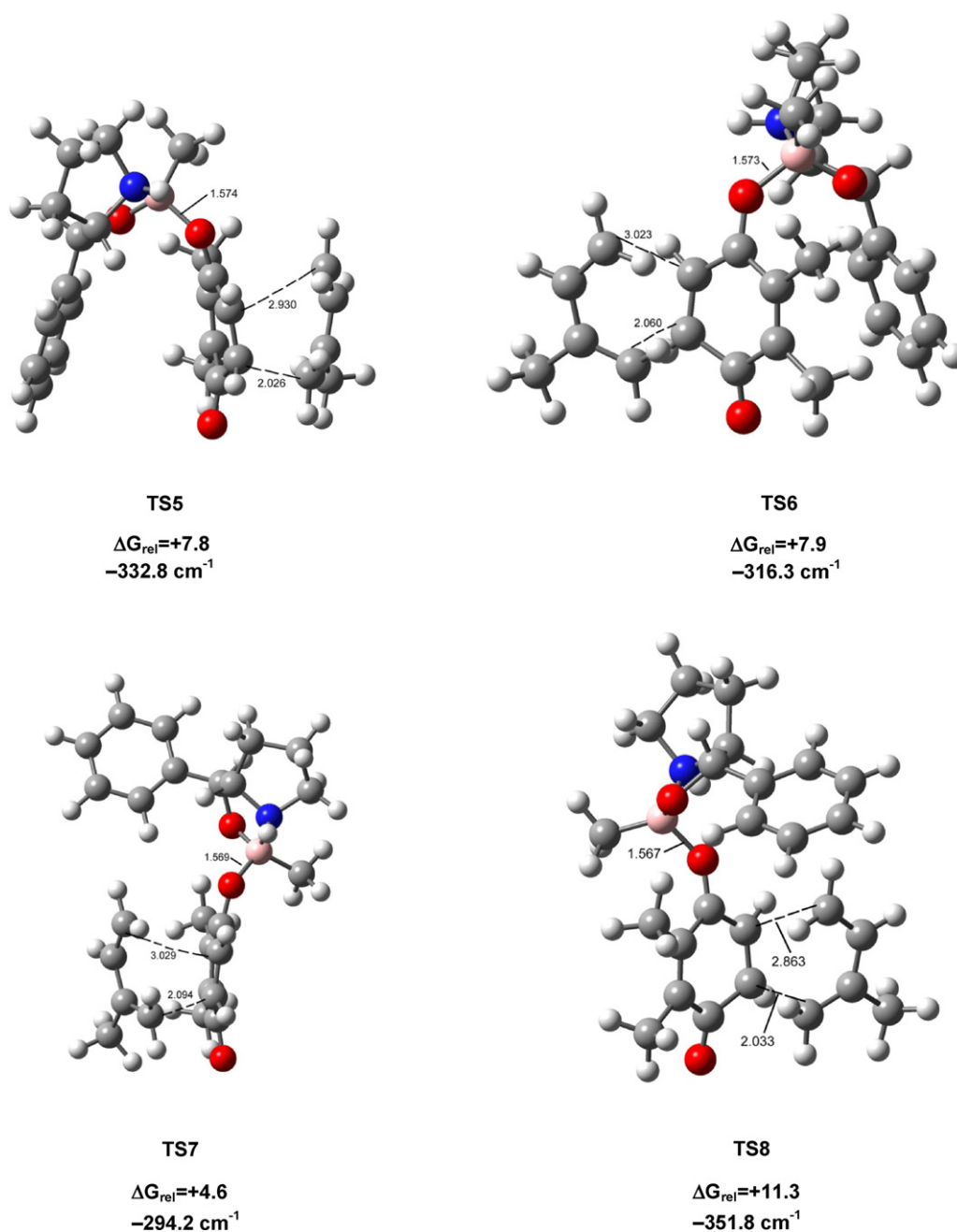
TS5

ΔG_{rel}=+7.8

−332.8 cm^{-1}

TS6

ΔG_{rel}=+7.9

−316.3 cm^{-1}

TS7

ΔG_{rel}=+4.6

−294.2 cm^{-1}

TS8

ΔG_{rel}=+11.3

−351.8 cm^{-1}

Fig. 6. (*Continued*).

slightly stronger complexation at the transition state. Similar to the reactant, the transition states possess a nonconventional hydrogen bond between the C_α–H hydrogen and the oxygen of the catalyst with bond lengths ranging from 2.15 Å to 2.61 Å.

TS10 possesses the lowest free energy representing almost a 100% of the Boltzmann population of the *endo* transition states. This transition state corresponds to diene addition to the rear face of the α,β double bond of the benzoquinone. For the *exo* transition states, **TS11** is the most stable transition state and represents 99.92% of the Boltzmann population of the *exo* transition states. The *endo* path is preferred to the *exo* route and the percent enantiomeric excess (%*ee*) is calculated to be 86.5%. These results are in agreement with those obtained for the homogeneous catalyst (Section 3.2) with the exception that the *endo* transition-state structure has

a preference for the rear face addition and the *exo* transition-state structure favors the front face addition.

Fig. 9 shows the reaction energy diagrams for the homogeneous (**TS1** (*endo*) and **TS4** (*exo*)) and the heterogeneous (**TS10** (*endo*) and **TS11** (*exo*)) Diels–Alder reactions at 298 K. As can be seen from the figure, the homogeneous Diels–Alder reaction is faster than the heterogeneous one by ~48 times.

The average degree of asynchronicity for the transition-state structures is found to be 0.99 Å (Fig. 8) pointing out to concerted but highly asynchronous reaction pathways where the bond between the diene and carbon β of the dienophile is being formed in a greater extent than the bond between the diene and carbon α of the dienophile. This is again similar to the results obtained for the homogeneous catalyst (Section 3.2).
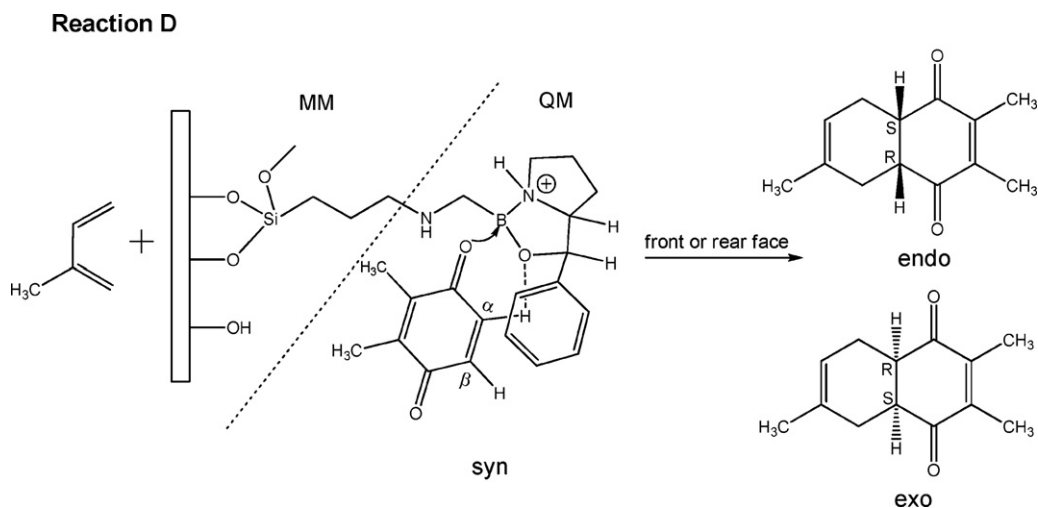
Reaction D

Fig. 7. Catalyzed Diels–Alder reaction with catalyst immobilized on amino SiO$_2$ surface having four possible reaction pathways. The catalyst is coordinated *syn* to the HC=CH double bond that undergoes the [4+2]-cycloaddition. The dotted line indicates the partitioning into MM and QM regions.
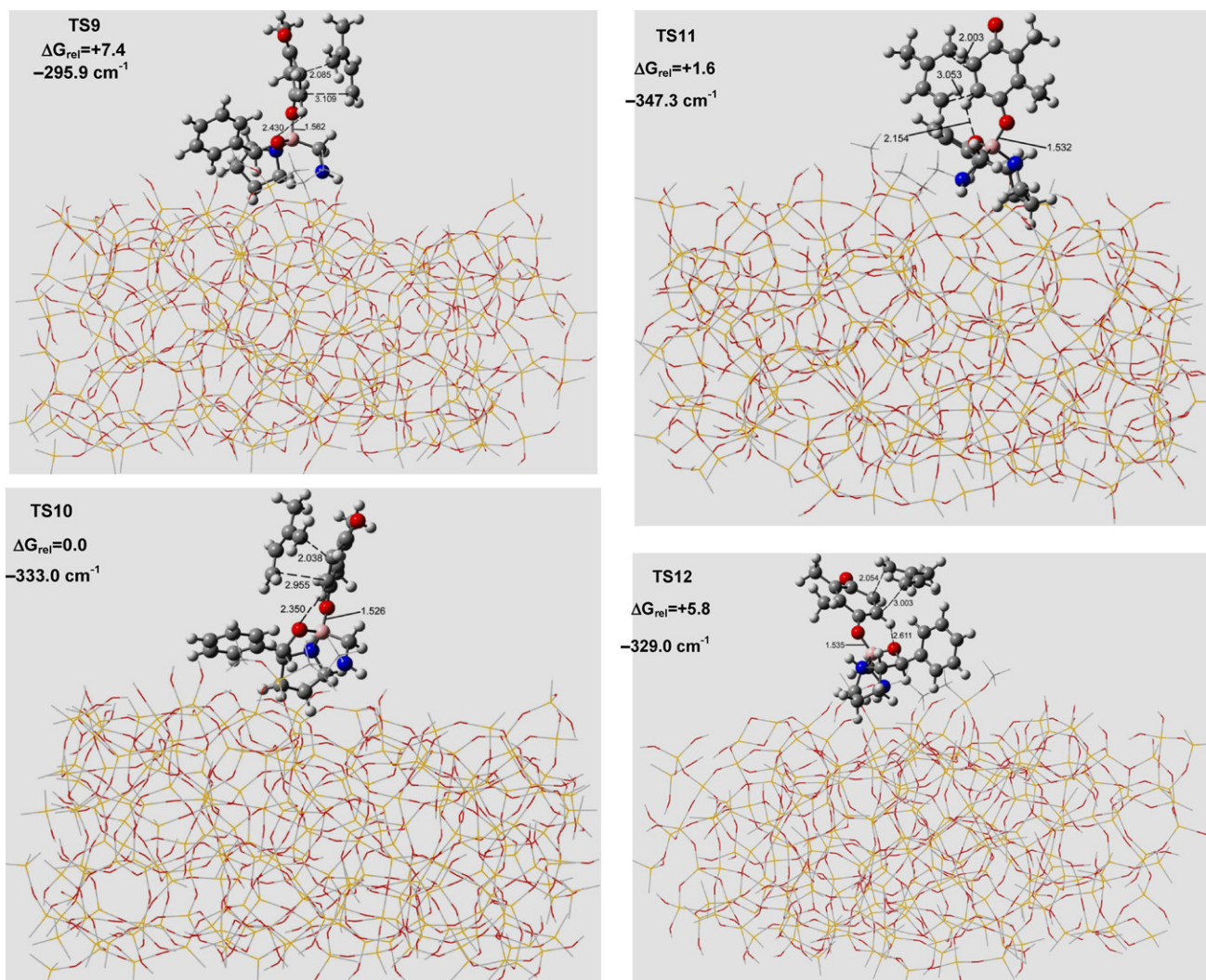

Fig. 8. ONIOM(B3LYP/6-31G(d):UFF) optimized transition-state structures for the catalyzed Reaction D. Relative free energies are in kcal/mol at 298 K and distances are in Å. **TS9** = *endo* transition state involving diene attack to the front face, **TS10** = *endo* transition state involving diene attack to the rear face, **TS11** = *exo* transition state involving diene attack to the front face and **TS12** = *exo* transition state involving diene attack to the rear face. The QM layer is in the ball-and-stick representation and the MM layer is in the wireframe representation. Negative wavenumbers are imaginary frequencies. The color code is the same as in Fig. 4.
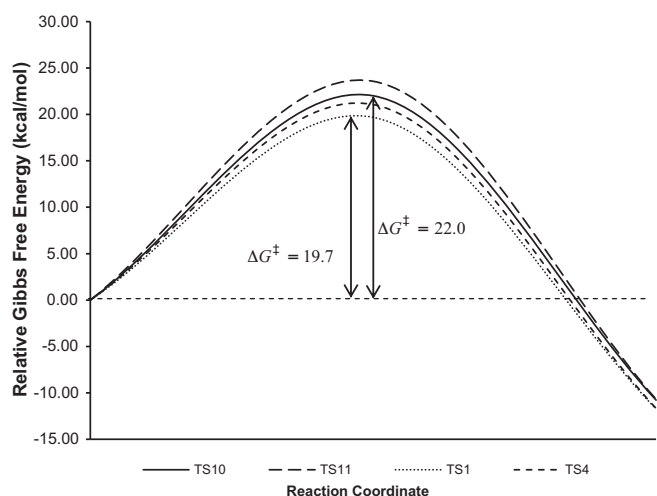
Fig. 9. Reaction energy diagrams for the homogeneous (**TS1** (*endo*) and **TS4** (*exo*)) and the heterogeneous (**TS10** (*endo*) and **TS11** (*exo*)) Diels–Alder reactions at 298 K. Activation free energies are in kcal/mol.

4. Conclusion

The Diels–Alder reaction between diene **1** and dienophile **2** in the presence of SiO_2-immobilized catalyst **4** has been studied by the hybrid ONIOM(B3LYP/6-31G(d):UFF) method within the mechanical embedding scheme. The amorphous silica surface was obtained by classical molecular dynamics using the melt-quench method. The silica surface was characterized and found to closely resemble silicas calcined at 673 K. The model chiral cationic oxazaborolidinium catalyst **4** was immobilized on the aminopropyl-functionalized silica surface to act as a heterogeneous catalyst for the Diels–Alder reaction. The preferred SiO_2-supported catalyst **4** coordination to dienophile **2** was observed to be *syn* to the HC=CH double bond of the dienophile that undergoes the [4+2]-cycloaddition. The favored reaction path was through an *endo* transition state and the calculated enantioselectivity was 86.5%. The reaction was observed to proceed via a concerted but highly asynchronous mechanism. The enantioselectivity and the mechanism of the Diels–Alder reaction on silica surface are generally comparable to those observed for the homogeneous catalyst.

References

[1] T. Leßmann, H. Waldmann, Chem. Commun. (2006) 3380–3389.
[2] F.Z. Dörwald, Organic Synthesis on Solid Phase: Supports, Linkers Reactions, Wiley-VCH, Weinheim, Germany, 2000.
[3] G.V. Smith, F. Notheisz, Heterogeneous Catalysis in Organic Chemistry, Academic Press, Burlington, MA, 1999.
[4] Science and technology in catalysis 2002, in: J.A.M. Brandts, E.G.M. Kuijpers, P.H. Berben, M. Anpo, M. Onaka, H. Yamashita (Eds.), Proceedings of the Fourth Tokyo Conference on Advanced Catalytic Science and Technology, Kodansha Ltd., Tokyo, Japan, 2003, pp. 451–454.
[5] T. Maschmeyer, L. van de Water, in: E.G. Derouane (Ed.), Catalysts for Fine Chemical Synthesis – Vol. 4 Microporous and Mesoporous Solid Catalysts, John Wiley & Sons, Ltd., Chichester, England, 2006, pp. 1–38.
[6] C.E. Song, S-G. Lee, Chem. Rev. 102 (2002) 3495–3524.
[7] C. Li, Catal. Rev. – Sci. Eng. 46 (2004) 419–492.
[8] R. Haag, S. Roller, Top. Curr. Chem. 242 (2004) 1–42.
[9] J. Horn, F. Michalek, C.C. Tzschucke, W. Bannwarth, Top. Curr. Chem. 242 (2004) 43–75.
[10] B.M.L. Dioos, I.F.J. Vankelecom, P.A. Jacobs, Adv. Synth. Catal. 348 (2006) 1413–1446.
[11] G.J. Meuzelaar, R.A. Sheldon, in: R.A. Sheldon, H. van Bekkum (Eds.), Fine Chemicals Through Heterogeneous Catalysis, Wiley-VCH, Weinheim, Germany, 2001, pp. 284–294.
[12] S. Itsuno, K. Watanabe, T. Koizumi, K. Ito, React. Polym. 24 (1995) 219–227.
[13] J.D. Winkler, W. McCoull, Tetrahedron Lett. 39 (1998) 4935–4936.
[14] D. Rechavi, M. Lemaire, Org. Lett. 3 (2001) 2493–2496.
[15] D. Rechavi, M. Lemaire, Chem. Rev. 102 (2002) 3467–3494.
[16] M. Tada, Y. Iwasawa, Chem. Commun. (2006) 2833–2844.
[17] S. Tanaka, M. Tada, Y. Iwasawa, J. Catal. 245 (2007) 173–183.
[18] J.M. Fraile, J.I. García, J.A. Mayoral, Coord. Chem. Rev. 252 (2008) 624–646.
[19] J.M. Fraile, J.I. García, C.I. Herrerías, J.A. Mayoral, E. Pires, L. Salvatella, Catal. Today 140 (2009) 44–50.
[20] K. Motokura, M. Tada, Y. Iwasawa, Catal. Today 147 (2009) 203–210.
[21] M.I. Burguete, J.M. Fraile, J.I. García, E. García-Verdugo, C.I. Herrerías, S.V. Luis, J.A. Mayoral, J. Org. Chem. 66 (2001) 8893–8901.
[22] A. Corma, H. García, A. Moussaif, M.J. Sabater, R. Zniber, A. Redouane, Chem. Commun. (2002) 1058–1059.
[23] L.-N. Huang, X.-P. Hui, Z.-C. Chen, C. Yin, P.-F. Xu, X.-X. Yu, S.-Y. Cheng, J. Mol. Catal. A: Chem. 275 (2007) 9–13.
[24] S. Doherty, P. Goodrich, C. Hardacre, V. Pârvulescu, C. Paun, Adv. Synth. Catal. 350 (2008) 295–302.
[25] C. McDonagh, P. O'Leary, Tetrahedron Lett. 50 (2009) 979–982.
[26] C. Franot, G.B. Stone, P. Engeli, C. Spöndlin, E. Waldvogel, Tetrahedron: Asymmetry 6 (1995) 2755–2766.
[27] M.D. Price, J.K. Sui, M.J. Kurth, N.E. Schore, J. Org. Chem. 67 (2002) 8086–8089.
[28] J.M. Fraile, J.A. Mayoral, J. Serrano, M.A. Pericàs, L. Solà, D. Castellnou, Org. Lett. 5 (2003) 4333–4335, http://pubs.acs.org/doi/abs/10.1021/ol0355985-ol0355985AF3.
[29] S. Degni, C.-E. Wilén, A. Rosling, Tetrahedron: Asymmetry 15 (2004) 1495–1499.
[30] D. Font, C. Jimeno, M.A. Pericàs, Org. Lett. 8 (2006) 4653–4655, http://pubs.acs.org/doi/abs/10.1021/ol061964j-ol061964jAF1.
[31] I. Hermans, J. van Deun, K. Houthoofd, J. Peeters, P.A. Jacobs, J. Catal. 251 (2007) 204–212.
[32] Y.-B. Zhao, L.-W. Zhang, L.-Y. Wu, X. Zhong, R. Li, J.-T. Ma, Tetrahedron: Asymmetry 19 (2008) 1352–1355.
[33] T. Miao, L. Wang, Tetrahedron Lett. 49 (2008) 2173–2176.
[34] J. Yune, K. Molvinger, F. Quignard, Catal. Today 138 (2008) 104–109.
[35] K. Ding, Y. Uozumi (Eds.), Handbook of Asymmetric Heterogeneous Catalysis, Wiley-VCH, Weinheim, Germany, 2008.
[36] U. Balakrishnan, N. Ananthi, S.T. Selvan, R. Pal, K. Ariga, S. Velmathi, A. Vinu, Chem. Asian J. 5 (2010) 897–903.
[37] E.J. Corey, Angew. Chem., Int. Ed. 48 (2009) 2100–2117.
[38] D.H. Ryu, E.J. Corey, J. Am. Chem. Soc. 125 (2003) 6388–6390.
[39] A.A. Selezenev, A.Y. Aleynikov, N.S. Gantchuk, P.V. Yermakov, J.K. Labanowski, A.A. Korkin, Comput. Mater. Sci. 28 (2003) 107–124.
[40] E.R. Cruz-Chu, A. Aksimentiev, K. Schulten, J. Phys. Chem. B 110 (2006) 21497–21508.
[41] X. Yang, Z. Xu, C. Zhang, J. Colloid Interface Sci. 297 (2006) 38–44.
[42] X. Yang, X. Yue, Colloids Surf. A 301 (2007) 166–173.
[43] F. Zipoli, D. Donadio, M. Bernasconi, J. Phys.: Condens. Matter 20 (2008) 224011.
[44] Y. Qin, X. Yang, Y. Zhu, J. Ping, J. Phys. Chem. C 112 (2008) 12815–12824.
[45] N.T. Huff, E. Demiralp, T. Çagin, W.A. Goddard III, J. Non-Cryst. Solids 253 (1999) 133–142.
[46] E. Demiralp, T. Çagin, W.A. Goddard III, Phys. Rev. Lett. 82 (1999) 1708–1711.
[47] A. Takada, P. Richet, C.R.A. Catlow, G.D. Price, J. Non-Cryst. Solids (2004) 224–229, 345&346.
[48] V.V. Hoang, N.T. Hai, H. Zung, Phys. Lett. A 356 (2006) 246–250.
[49] T. Yoshioka, A. Yasumoto, K. Kishi, T. Tsuru, Desalination 233 (2008) 333–341.
[50] B.W.H. van Beest, G.J. Kramer, R.A. van Santen, Phys. Rev. Lett. 64 (1990) 1955–1958.
[51] K. Vollmayr, W. Kob, K. Binder, Phys. Rev. B 54 (1996) 15808–15827.
[52] J. Horbach, W. Kob, Phys. Rev. B 60 (1999) 3169–3181.
[53] A. Carré, L. Berthier, J. Horbach, S. Ispas, W. Kob, J. Chem. Phys. 127 (2007), 114512-1-9.
[54] Y. Wang, X. Xu, L. Zheng, Appl. Phys. A: Mater. Sci. Process 92 (2008) 849–852.
[55] V.A. Bakaev, Phys. Rev. B 60 (1999) 10723–10726.
[56] S. von Alfthan, A. Kuronen, K. Kaski, Phys. Rev. B 68 (2003) 073203–73214.
[57] E.A. Leed, C.G. Pantano, J. Non-Cryst. Solids 325 (2003) 48–60.
[58] E.J. Corey, T. Shibata, T.W. Lee, J. Am. Chem. Soc. 124 (2002) 3808–3809.
[59] D.H. Ryu, T.W. Lee, E.J. Corey, J. Am. Chem. Soc. 124 (2002) 9992–9993.
[60] G. Zhou, Q.-Y. Hu, E.J. Corey, Org. Lett. 5 (2003) 3979–3982.
[61] D.H. Ryu, G. Zhou, E.J. Corey, J. Am. Chem. Soc. 126 (2004) 4800–4802.
[62] D.H. Ryu, E.J. Corey, J. Am. Chem. Soc. 127 (2005) 5384–5387.
[63] D.H. Ryu, G. Zhou, E.J. Corey, Org. Lett. 7 (2005) 1633–1636.
[64] D. Liu, E. Canales, E.J. Corey, J. Am. Chem. Soc. 129 (2007) 1498–1499.
[65] Q.-Y. Hu, G. Zhou, E.J. Corey, J. Am. Chem. Soc. 126 (2004) 13708–13713.
[66] M.J. Frisch, G.W. Trucks, H.B. Schlegel, G.E. Scuseria, M.A. Robb, J.R. Cheeseman, J.A. Montgomery Jr., T. Vreven, K.N. Kudin, J.C. Burant, J.M. Millam, S.S. Iyengar, J. Tomasi, V. Barone, B. Mennucci, M. Cossi, G. Scalmani, N. Rega, G.A. Petersson, H. Nakatsuji, M. Hada, M. Ehara, K. Toyota, R. Fukuda, J. Hasegawa, M. Ishida, T. Nakajima, Y. Honda, O. Kitao, H. Nakai, M. Klene, X. Li, J.E. Knox, H.P. Hratchian, J.B. Cross, V. Bakken, C. Adamo, J. Jaramillo, R. Gomperts, R.E. Strat-

mann, O. Yazyev, A.J. Austin, R. Cammi, C. Pomelli, J.W. Ochterski, P.Y. Ayala, K. Morokuma, G.A. Voth, P. Salvador, J.J. Dannenberg, V.G. Zakrzewski, S. Dapprich, A.D. Daniels, M.C. Strain, O. Farkas, D.K. Malick, A.D. Rabuck, K. Raghavachari, J. B. Foresman, J.V. Ortiz, Q. Cui, A.G. Baboul, S. Clifford, J. Cioslowski, B.B. Stefanov, G. Liu, A. Liashenko, P. Piskorz, I. Komaromi, R.L. Martin, D.J. Fox, T. Keith, M.A. Al-Laham, C.Y. Peng, A. Nanayakkara, M. Challacombe, P.M.W. Gill, B. Johnson, W. Chen, M.W. Wong, C. Gonzalez, J.A. Pople, Gaussian 03, Revision E.01, Gaussian, Inc., Wallingford CT, 2004.

[67] L.J. Broadbelt, R.Q. Snurr, Appl. Catal., A 200 (2000) 23–46.
[68] HyperChem(TM), Hypercube, Inc., 1115 NW 4th Street, Gainesville, Florida 32601, USA.
[69] A.K. Rappé, C.J. Casewit, K.S. Colwell, W.A. Goddard III, W.M. Skiff, J. Am. Chem. Soc. 114 (1992) 10024–10035.
[70] A.K. Rappe, W.A. Goddard III, J. Phys. Chem. 95 (1991) 3358–3363.
[71] K. Gundertofte, T. Liljefors, P.-O. Norrby, I. Pettersson, J. Comput. Chem. 17 (1996) 429–449.
[72] Molecular Mechanics Methods, http://www.gaussian.com/g_tech/g_ur/k_mm-.htm (accessed March 2010).
[73] Y.V. Joshi, K.T. Thomson, J. Catal. 230 (2005) 440–463.

[74] M. Lundberg, T. Kawatsu, T. Vreven, M.J. Frisch, K. Morokuma, J. Chem. Theory Comput. 5 (2009) 222–234.
[75] T. Vreven, K. Morokuma, Ö. Farkas, H.B. Schlegel, M.J. Frisch, J. Comput. Chem. 24 (2003) 760–769.
[76] H.E. Bergna, in: H.E. Bergna, W.O. Roberts (Eds.), Colloidal Silica: Fundamentals and Applications, CRC Press, Boca Raton, FL, 2006, pp. 9–35.
[77] Y. Iwasawa, in: Y. Iwasawa (Ed.), Tailored Metal Catalysts, D. Reidel Publishing Company, Dordrecht, Holland, 1986, pp. 1–85.
[78] R.T. Yang, Adsorbents: Fundamentals and Applications, John Wiley & Sons, Inc., Hoboken, NJ, 2003.
[79] M. Alkam, M. Dogan, in: P. Somasundaran (Ed.), Encyclopedia of Surface and Colloid Science, CRC Press, Boca Raton, FL, 2006, pp. 5608–5620.
[80] Sigma–Aldrich, Product Number: 364258, Product Name: 3-aminopropyl-functionalized silica gel, http://www.sigmaaldrich.com/catalog/AdvancedSearchPage.do (accessed March 2010).
[81] E.J. Corey, T.W. Lee, Chem. Commun. (2001) 1321–1329.
[82] M.D. Mackey, J.M. Goodman, Chem. Commun. (1997) 2383–2384.
[83] S. Kong, J.D. Evanseck, J. Am. Chem. Soc. 122 (2000) 10418–10427.
[84] D.M. Birney, K.N. Houk, J. Am. Chem. Soc. 112 (1990) 4127–4133.